Plasma activation of CO_2 in a dielectric barrier discharge: a chemical kinetic model from the microdischarge to the reactor scales

Martin Alliati, Danhua Mei, Xin Tu[1]

Department of Electrical Engineering and Electronics, University of Liverpool,

Liverpool L69 3GJ, UK

Abstract

The conversion of CO_2 into value-added chemicals or fuels has attracted much attention over the past years. Plasma technology represents a highly promising alternative due to its non-equilibrium nature, deemed crucial for CO_2 dissociation reactions. Gaining a deep understanding of the reaction mechanisms involved under plasma conditions is essential to improve the performance of such processes. Among other theoretical calculations, plasma chemical kinetic modelling constitutes a very suitable approach to address this challenge. In this work, a zero-dimensional model of a dielectric barrier discharge (DBD) reactor is applied to CO_2 splitting, providing a novel approach for including experimental parameters as discharge power and flow rate based on the analysis of the different scales involved. The model choices is extensively discussed as regards experimental parameters, cross-section data and the chemical reactions considered. The predictions of the model are in good agreement with existing experimental data and therefore the model is considered valid to analyse the CO_2 splitting reaction mechanism based on its results. It is concluded that the electron impact dissociation is the dominant process towards CO_2 conversion, which could explain the low energy efficiency achieved since only ~10% of the electron energy is consumed by mechanism. The remaining energy would be lost towards vibrational excitation not leading to CO_2 dissociation in DBD reactors.

Keywords: Dielectric barrier discharge; Non-thermal plasma, CO_2 conversion, Plasma chemical kinetic modelling; Reaction pathways.

[1] Corresponding author, xin.tu@liverpool.ac.uk

1. Introduction

Turning CO_2 into a valuable feedstock by the development of new processes for its conversion to value added chemicals or fuels constitutes a major challenge already being addressed by scientists and engineers all over the world. The large amounts of CO_2 emitted on a daily basis due to the burning of fossil fuels account for the availability of this molecule. In addition, these anthropogenic CO_2 emissions must be reduced due to their effect as a greenhouse gas, as well as their negative impact in terms of global warming [1]. For these reasons, CO_2 splitting has attracted great attention over the past years among scientists within the fields of sustainability, renewable energy and environmental sciences [2–11].

Unfortunately, CO_2 is a highly stable molecule ($\Delta G° = -394\ kJ/mol$) and its dissociation is strongly endothermic ($\Delta H° = +283\ kJ/mol$) [2]. Hence, high conversions are not easy to achieve without a fairly poor energy efficiency. Many research efforts have aimed to overcome these difficulties, among which plasma processing is presented as a promising alternative due to their non-equilibrium nature [13–25]. Electron impact reactions provide unique mechanisms for CO_2 dissociation that can take place at room temperature and atmospheric pressure, this being a major advantage of non-thermal plasma technologies in comparison with other methods like thermal catalysis [1]. Also, turning a plasma system on and off is relatively straightforward, which makes it the ideal complement to the promising yet fluctuating renewable energy sources [2].

Dielectric barrier discharge (DBD) reactors have been extensively studied for CO_2 conversion, partially due to their simplicity [13–25]. These types of reactors normally operate at atmospheric pressure and near room temperature. Moreover, they have a simple design suitable for industrial scales and a catalyst can be easily incorporated [14,17–25]. The energy efficiency of CO_2 splitting reactions in DBD reactors (typically below 10% at atmospheric pressure [26,27]) needs further improvement for this technology to be industrially relevant. In terms of syngas production from CO_2 reforming of methane, DBD reactors should reach an energy efficiency of around 60% to be competitive with both existing and emerging technologies. This target can be reduced by a factor of 2 or 3 for direct oxidative pathways towards liquid products, which is closer to the currently achieved energy efficiency [2].

In the quest for improving the energy efficiency, understanding the reaction mechanisms of CO_2 conversion is of major importance [2]. Numerical modelling seems to be the best approach for revealing the underlying chemistry of this system. Among these simulations, plasma kinetic modelling provides a great tool to analyse the relevance of various processes leading to CO_2 conversion. Due to the high computational cost of fluid models, non-dimensional models have been developed and applied to DBD reactors, yielding reasonable agreement with experimental data in most cases [28–35].

In this study, calculations based on a zero-dimensional plasma kinetic model of CO_2 splitting in a tubular DBD reactor are performed and the results are compared with existing experimental data [36]. Once validated, the model is used to understand the reaction mechanisms involved based on its results. A novel approach to the already existing DBD reactor zero-dimensional models is presented in order to incorporate the effect of the main experimental parameters in the CO_2 conversion, namely discharge power and flow rate. To the best of our knowledge, some important considerations and approximations included in the model have never been tested before. A discussion of the most suitable cross sections datasets for the electron impact dissociation is also presented based on results reported elsewhere [32,37]. Polak and Slovetsky's CO_2 dissociation total cross section data [38] was finally selected to calculate the CO_2 electron impact dissociation rate coefficient, being contrasted to experimental results in terms of CO_2 conversion for the first time. A reduced chemistry set reported in [31] is employed for this model, also contributing towards a low computational cost as it only involves 17 reactions and 9 species. A reduced electric field (E/N) well outside the range of figures reported elsewhere for DBD reactors is used. This might have important consequences regarding the main channels for CO_2 dissociation and the energy efficiency achieved in DBD reactors in comparison with that of microwave (MW) discharges. Calculations were performed by means of the ZDPlasKin Fortran module (version 2.0a, Sep 2017) [39]. BOLSIG+ solver (version 03/2016) was employed to calculate the rate coefficients of the electron impact reactions [40]. LXCat project databases were used for retrieving cross section data [41].

2. Description of the model

2.1. Experimental setup to be modeled

According to the experiments that the model in this study intends to represent, a co-axial DBD reactor with no packing will be considered (see Figure 1). In every case relevant to this work, the discharge length is 100 mm while there is a 2.5 mm discharge gap (the inner diameter of the quartz tube is 22 mm while the outer diameter of the inner electrode is 17 mm). Further details on the experimental setup can be found in our previous work [36]. Different values for the discharge power and flow rate are considered (10 to 50 W and 25 to 125 mL/min, respectively), corresponding to different experimental measurements. The voltage across the gap has been calculated through Lissajous figures, leading to a reduced electric field of 56 Td. This value will be used as an input parameter throughout all the calculations performed in this work. For further information on the method used to calculate E/N from Lissajous figures, see ref [42].

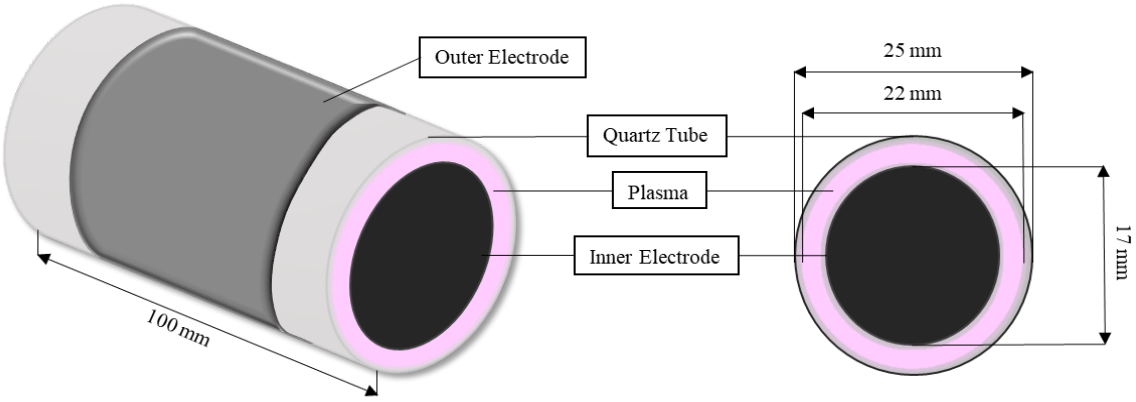

Figure 1 – Schematic diagram of DBD plasma reactor

2.2. Zero-dimensional DBD reactor model

Zero-dimensional models have been previously applied to plasma kinetic modelling of DBD reactors[28–31]. The main simplification of these models relies on neglecting any spatial variations of any property in the radial and angular coordinates of the tubular reactor, i.e. properties only vary along the axial coordinate of the reactor (Z). Like in plug flow models of tubular reactors, a *slice of reactor* with a differential length dZ can be considered as a differential element of volume within which every property is homogeneous. The *slice of*

reactor flows through the reactor from Z=0 to L (reactor length) with an average velocity $\langle V \rangle$, considered to be homogeneous in the reactor's flow section for the purpose of this model (planar velocity profile). In addition, this magnitude is assumed to be constant along the axial coordinate since density (temperature and pressure) variations between the reactor's inlet and outlet are neglected. Therefore, the velocity is essentially the ratio between the reactor length (L) and its residence time (θ). In fact, this model become non-dimensional when the independent variable Z is translated into the residence time (θ). Each element of volume flowing through the reactor (Z = 0 to L) can be seen as a small batch reactor progressing in time until reaching the residence time of the reactor (t = 0 to θ). Then, as expressed in equation 1, the j^{th} production or loss process will contribute to the variation of the number density of the i^{th} species (N_i) with respect to residence time according to the stoichiometric coefficient of the i^{th} species in the j^{th} reaction (a_{ij}) and its reaction rate (rrt_j). See variable index in Table S3.

$$\frac{dN_i}{d\theta} = \sum\nolimits_j a_{ij} \times rrt_j \; = \; \sum\nolimits_j a_{ij} \times k_j \times \prod\nolimits_l N_i \quad (1)$$

Plasma discharges in DBD reactors present a filamentary regime for most gases and it is certainly the case for CO_2 [43]. Therefore, the element of volume described above passes through a number of filaments as it flows through the reactor, facing a high concentration of plasma electrons which in turn generate short lived plasma species by electron impact reactions. In terms of the non-dimensional model, these filaments, which are spatially spread along the axial coordinate of the reactor, can be represented as consecutive pulses over time with a certain frequency (f_{pulses}) [29]. This parameter has been widely varied among the different zero-dimensional models published in the past years, ranging from values in the order of the actual voltage frequency (tens of kHz) [29] to arbitrarily chosen values like 1000 kHz [28] or 0.03 kHz [31]. Interestingly, this frequency of pulses in the model is not strongly related to the actual frequency of the voltage applied to the plasma system. In fact, it can be understood in terms of the period resulting from the ratio of the distance between two consecutive filaments ($\Delta Z_{fil-to-fil}$) and the velocity of the fluid ($\langle v \rangle$). That is to say, the frequency of the pulses in the zero-dimensional model can be expressed as in equation 2, where $\langle v \rangle$ is the average velocity of the fluid inside the reactor and $\Delta Z_{fil-to-fil}$ is the space

between two consecutive filaments (see Figure 2). Notably, the latter quantity brings uncertainty into the model. However, this reasoning gives a much narrower range of reasonable values for the frequency of pulses, within which it is just a fitting parameter.

$$f_{pulses} = \frac{1}{\Delta t_{fil-to-fil}} = \frac{\langle v \rangle}{\Delta Z_{fil-to-fil}} \quad (2)$$

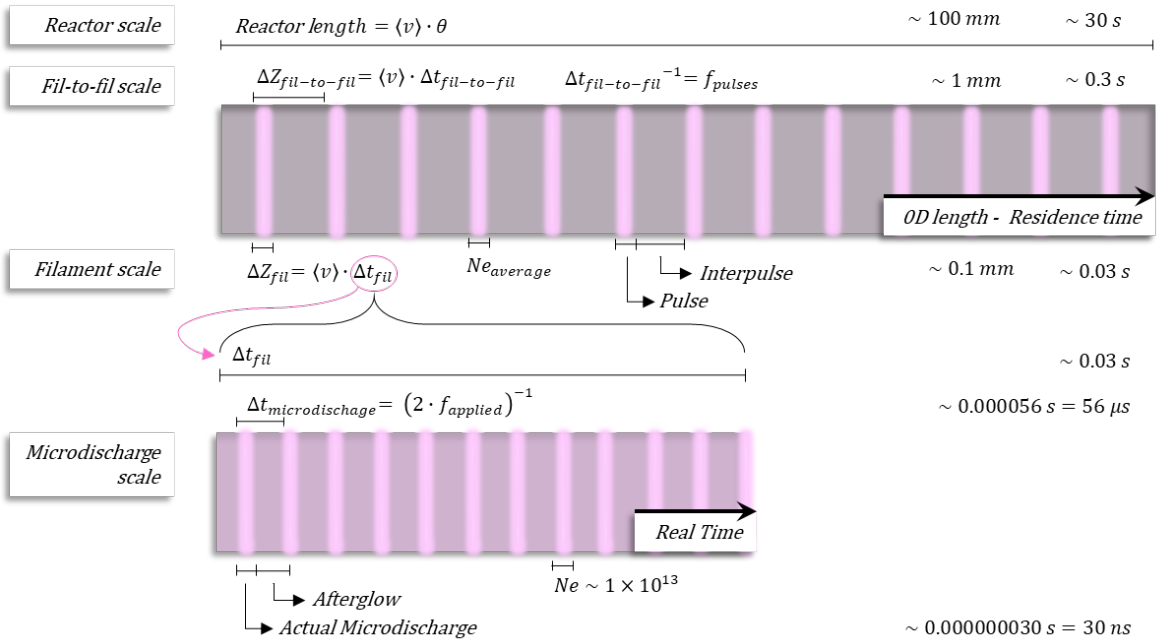

Figure 2 – Scales and parameters in the model of a DBD reactor

2.3. Effect of power in the model's parameters – *filament-to-filament scale*

Mei et al. showed experimentally that the power deposited on the plasma system affects the conversion of CO_2 [36]. In the referred work, a range of power values from 10 to 50 W was covered resulting in an increase from 17.4 to 22.4% in the CO_2 conversion. Furthermore, we consider the electric field must remain constant regardless of the power value, as the breakdown voltage should as well (56 Td for all calculations in this work, as measured applying the methodology in [42] to the experimental setup of [36]). However, an increase in the power does cause a rise in the number of filaments per unit area observed in the system, as reported in [44]. Model wise, we propose to take this effect into consideration to account

for the rise in conversion with power. Ultimately, a greater number of filaments implies a shorter spacing $\Delta Z_{fil-to-fil}$ and so a higher frequency of pulses f_{pulses} for the same velocity of the fluid. In other words, this implies more pulses in the same residence time and, hence, a greater conversion.

The spacing between filaments is not known and a reference value of 1 mm was proposed for this model based on experimental observations. Then, this magnitude should be slightly above or below that figure for lower or higher power deposition figures, respectively. Therefore, a dependence between $\Delta Z_{fil-to-fil}$ and the power has been proposed (equation 3) according to the relationship found experimentally between power and conversion [36].

$$\Delta Z_{fil-to-fil} = \frac{1\ mm}{K_p \times P^a} \quad (3)$$

The values of K_p and a are parameters to be found by minimising the difference between experimental and theoretical conversion values for every power value. In this way, $\Delta Z_{fil-to-fil}$ and consequently f_{pulses} constitutes the first fitting parameter of this model, as in other zero-dimensional models [29–31,34].

2.4. Effect of flow rate in the model's parameter – *one-filament scale*

As it has been shown experimentally, the flow rate has an inverse effect on the conversion, yielding lower CO_2 conversion at higher flow rates [36]. To start with, a higher flow rate results in both a shorter residence time (θ) and a higher frequency of pulses (f_{pulses}). These effects cancel out and the resulting number of pulses (num_{Pulses}) remains the same regardless of the flow rate, as can be seen in equation 4, where the residence time of the reactor can be expressed as $\theta = \frac{Reactor\ Volume}{Flowrate} = \frac{L}{\langle v \rangle}$ (see Figure 2).

$$num_{Pulses} = f_{pulses} \times \theta = \frac{\mathrm{L}}{\Delta Z_{fil-to-fil}} \quad (4)$$

Thus, the above described effects cannot explain the drop in conversion on its own and a closer look at a filament is needed to address the effect of a reduction in the flow rate. In this model, the space between filaments ($\Delta Z_{fil-to-fil}$) consists of a filament and a non-

filamentary region (interpulse), as shown in Figure 2. In the filament, molecules experience collisions with plasma electrons and electron impact reactions occur giving rise to more free electrons and reactive plasma species. On the other hand, ground state chemistry dominates in the interpulse since no plasma electrons are present and the short lived plasma species tend to be rapidly consumed in recombination reactions. Hence, the pulses (where free electrons are available) are what really drives the conversion of CO_2 in our model.

Although the number of pulses remains the same for every flow rate, it can be seen intuitively that each pulse is shorter lived at higher flow rates. In fact, the duration of both the pulse and the interpulse decrease at higher flow rates. However, as the CO_2 number density remains steady during the interpulse, a shorter interpulse does not have a noticeable impact in the conversion. By contrast, a lower duration of the pulse has a big impact in the CO_2 number density variation, resulting in a smaller overall CO_2 conversion for the same number of pulses.

The time during which an element of volume *sees* the pulse depends on the width of the filament and the velocity of the fluid, i.e., the flow rate. The filament width (ΔZ_{fil}) has been reported to range from 0.1 to 0.2 mm [43], so it should be noted that there is roughly an order of magnitude between that figure and the space between two consecutive filaments $\Delta Z_{fil-to-fil}$. Then, there is also an order of magnitude between the period between filaments ($\Delta t_{fil-to-fil}$, which determines the frequency of pulses f_{pulses} and the number of pulses num_{Pulses} given a residence time θ) and the duration of one filament (Δt_{fil}, which drives the CO_2 conversion for a given number of pulses num_{Pulses}). Besides, the duration of a filament in the zero-dimensional model could be expressed as $\Delta t_{fil} = \frac{\Delta Z_{fil}}{\langle v \rangle}$.

However, the above stated expression for Δt_{fil} predicts much greater conversion drops than those observed experimentally when increasing the flow rate. For this reason, in this study we suggest a balancing effect for this relation, proposing that the filament width depends on the velocity for the reasons exposed as follows.

First, let's consider the mechanisms that allow filaments to appear in a DBD reactor. Filaments are actually a group of micro-discharges that occur in the same spot every time the polarity of the electrodes changes. A micro-discharge lasts for tens of nanoseconds (ns)

before the electrons reach the positive electrode and the accumulated charge makes the local electric field collapse [43]. A filament duration of 30 ns has been repeatedly reported in the literature [28–34]. After a polarity reversal occurs, the deposited charge facilitates the formation of a new micro-discharge in the same spot. Although electrons dissipate in tens of nanoseconds, it takes tens of micro seconds (μs) for slow-moving heavy ions to reach the negative electrode, resulting in a low but long-lasting falling ion current. Hence, both the accumulated negative charge and the ion current characterises this region in space as a micro-discharge remnant, after a micro-discharge occurred. With a frequency of 9 kHz, a voltage polarity reversal occurs every 56 μs. The fact that the micro-discharge remnant is not fully dissipated before the polarity changes also facilitates the formation of a new micro-discharge in the same spot. This is called *memory effect* and explains why it is actually possible to see filaments in a DBD reactor. If the micro-discharges were formed on a new spot every time the polarity changed, the discharge would appear uniform and no spatially localised single filaments could be observed [43].

For the purpose of this model, we will analyse what impact could the flow regime have on the memory effect. As the flow regime changes from laminar to turbulent, velocity profiles inside the reactor tend to become planar. This is a result of more random particle displacements and a higher dispersion that tends to make properties homogeneous inside a *slice of reactor*, including the velocity. Thus, a more turbulent flow regime could slightly disperse the ions in the microdischarge remnant. Also, the velocity in the proximity of the inner walls of the reactor is higher in turbulent flow, as the velocity profile becomes planar. This could have an impact on how electrons are deposited in the positive electrode, enhancing dispersion as they move towards the electrode and giving the deposited electrons a wider spread over the cathode surface. All these dispersion effects could very slightly affect the memory effect of the micro-discharges. This effect might be very small as filaments are indeed observed for every flow rate, but it could be understood as a minimal step towards homogenizing the discharge (which would be the result of having no memory effect at all). Nevertheless, this effect could suffice to slightly disperse the micro-discharge remnant and moderately widen the spot where a next micro-discharge could occur, hence resulting in an enlargement of the filament width.

Based on this hypothesis, we propose a dependence between the filament width and the velocity of the fluid, which has an effect in the time a molecule spends in a filamentary region (duration of the pulse in terms of the model, Δt_{fil}). As stated above, the duration of the pulse has a great impact on the CO_2 conversion and it is what really drives the results for a constant number of pulses, num_{Pulses}. Therefore, equations 5 and 6 are proposed, where the values of K_v and b are parameters to be found by minimizing the difference between experimental and theoretical conversion figures for every flow rate value.

$$\Delta Z_{fil} = K_v \times \langle v \rangle^b \quad (5)$$

$$\Delta t_{fil} = \frac{\Delta Z_{fil}}{\langle v \rangle} = \frac{K_v \times \langle v \rangle^b}{\langle v \rangle} \quad (6)$$

Hence, as long as b is positive and smaller than 1, this effect could moderate the negative effect that a higher velocity has on the conversion values predicted by the model. In this way, the duration of the pulse Δt_{fil} (or the width of the filament, ΔZ_{fil}) works as the second fitting parameter of this model.

2.5. Electron density in one filament – *micro-discharge scale*

Considering the velocity of the fluid and the width of one filament, the time spent by a molecule inside the filament (model-wise, the duration of the pulse Δt_{fil}) ranges from around 15000 to 37000 μs. In that period of time, around 300 to 700 micro-discharges occur, as the frequency of the applied voltage is 9 kHz. This means, there is one micro-discharge every 56 μs ($\Delta t_{micro-discharge}$), each of them consisting of 30 ns of an actual micro-discharge (electron avalanche and plasma channel) plus an afterglow until the next micro-discharge. In our model, this happens every time the element of volume passes through a filament (that is num_{pulses} times). See Figure 2 for a comparison between the different scales involved.

For this behaviour to be computationally represented, a time step in the order of a fraction of a nanosecond would be needed. Then, it would require around 10^{10} time-steps numerically integrated to build up to a residence time of around tens of seconds. For this reason, the hundreds of micro-discharges taking place when the element of volume passes through a

filament will be averaged over the period of time inside that filament Δt_{fil}. The purpose of this simplification is to obtain an average electron density Ne_{av} valid for the whole period inside the filament, Δt_{fil}. Then, the number of micro-discharges in one filament can be expressed as in equation 7, leading to equation 8 for Ne_{av}.

$$num_{micro-discharges} = \Delta t_{fil} \times 9\ kHz \times 2_{half-cycles} = \frac{\Delta t_{fil}}{\Delta t_{micro-discharge}} \quad (7)$$

$$\int_0^{\Delta t_{fil}} Ne_{av}\, dt = num_{micro-discharges} \times \int_0^{\Delta t_{micro-discharge}} Ne(t)\, dt \quad (8)$$

As stated above, the plasma electrons during a micro-discharge are considered to last for around 30 ns [43], peaking somewhere in that interval and becoming zero from 30 ns onwards until the next micro-discharge (until $\Delta t_{micro-discharge}$ is reached). According to the literature, the electron density Ne can reach values around 10^{12}-10^{14} cm^{-3} [43]. Thus, the electron density in one micro-discharge will be modeled as a function of time standing at 0 cm^{-3} at 0 ns, promptly reaching a maximum of 1×10^{13} cm^{-3} at 3 ns and subsequently falling steadily to 0 cm^{-3} at 30 ns ($Ne(t)$). Then, the right hand side of equation 8 would modify as in equation 9.

$$\int_0^{\Delta t_{fil}} Ne_{av}\, dt = num_{micro-discharges} \times \left[\int_0^{30\ ns} Ne(t) dt + \int_{30\ ns}^{\Delta t_{micro-disc.}} 0\ dt \right] \quad (9)$$

From then on, an average electron density that is valid for the duration of one filament in our model (Δt_{fil}) can be obtained as expressed in equations 10 and 11.

$$Ne_{av} \cdot \Delta t_{fil} = num_{micro-discharges} \times \left[\int_0^{30\ ns} Ne_{micro-disc.}(t) dt \right] \quad (10)$$

$$Ne_{av} = \frac{1}{\Delta t_{micro-discharge}} \times \left[\int_0^{30\ ns} Ne_{micro-disc.}(t) dt \right] \quad (11)$$

In this way, an average electronic density of 4×10^{9} cm^{-3} is obtained, which will be considered constant for the duration of the pulse in our model (Δt_{fil}, which as it has been said, involves thousands of micro-discharges). This value will be used for all calculations over the range of power and flow rate values covered in this study. It should be noted that this value depends

on the duration of the pulse (30 ns) and $\Delta t_{micro-discharge}$ (which depends on the frequency of the applied voltage, 9 kHz) rather than on Δt_{fil}.

To the best of our knowledge, an electron density of 1×10^{13} cm^{-3} is a reasonable value to base our approximation on as it is within the range of values reported for DBD reactors 10^{12}-10^{14} cm^{-3}. Furthermore, values in this region have been used in several published modelling works [28–34]. However, our calculated conversion is very sensible with respect to the electron density. Hence, the latter is acting as a third fitting parameter of our model, even though it is not intended to. This leads to a discussion about what a relatively arbitrarily chosen electron density means for the simulation. Several plasma phenomena lie under this umbrella over which we do not have control and cannot model accurately. Moreover, even if we could measure the electron density precisely, the only way we could account for those phenomena is to have an average electron density that yields good agreement with the experiments in terms of CO_2 conversion.

For these reasons, we consider this approach acceptable as long as the electron density fits within the reported values for DBD reactors. From a maximum electron density of 1×10^{13} cm^{-3}, the average electron density of 4×10^{9} cm^{-3} arises. It should be mentioned that the exact same figure has been used for all calculations in this work.

2.6. Summary of the reactor model

For the reasons exposed above, our model consists of a number of pulses (num_{pulses}) that occur every $\Delta t_{fil-to-fil}$ seconds. Each pulse will have a constant electronic density $Ne_{average}$ held for Δt_{fil} and an interpulse of around ($\Delta t_{fil-to-fil} - \Delta t_{fil}$) seconds with no plasma electrons, until the element of volume reaches the next filament or pulse (see Figure 2). This new approach implies a very low computational cost, which allows us to perform calculations effectively (typically in the order of hours of computational time). Table S1 summarises the parameters of each calculation performed in this work.

As described above, the unknown physical aspects of a DBD discharge lead to the three fitting parameters of this model, namely, the frequency of pulses (f_{pulses}), the duration of the

pulse (Δt_{fil}) and the average electron density (Ne_{av}). The former is related to the spacing between filaments $\Delta t_{fil-to-fil}$ and represents the effect of the discharge power in the conversion of CO_2. The second fitting parameter represents the time spent by a molecule inside a filament and depends on the fluid velocity or flow rate. Notably, the ratio between Δt_{fil} and $\Delta t_{fil-to-fil}$ is equal to that between the plasma volume and the total reactor volume. At this point, it should be highlighted that this selection of fitting parameters is equivalent to that of other zero-dimensional models [29–34]. However, the way in which these fitting parameters are derived in our model results in a narrower range of reasonable values for them (no more than one order of magnitude in both cases).

Finally, the electron density is not intended as a fitting parameter, however it should be regarded as such since the conversion predicted by the model is very sensitive to it. Although this limits the reliability on our model, there is no further improvement we could do at the moment. The average electron density is calculated considering a maximum electron density of 1×10^{13} cm^{-3} and a micro-discharge duration of 30 ns. Both values agree with the state of the art of plasma kinetic modelling of DBD reactors [29–35].

2.7. Chemical model

For the chemical model, a reduced set of reactions developed and reported in [31] was employed. This reduced set consists of 9 species (see Table S2) and 17 reactions, which implies a much lower computational cost than the complete set (around 42 species and 500 reactions) [28,31,33]. The reactions considered, shown in Table 1, involve 7 electron impact reactions (R1 to R7), as well as 5 reactions among ions (R8 to R12) and 5 between neutral species (R13 to R16). As regards CO_2 conversion by electron impact reactions, the main mechanisms identified in [28] are taken into account, i.e., electron attachment (R1), electron impact dissociation (R2) and total ionisation (R3). Vibrationally excited states of CO_2 were not taken into account in this model for the reasons presented in Section 0.

In addition, Electron impact dissociation reactions were considered for O_3 and O_2 (R4 and R5, respectively), while for the latter two electron attachment reactions were also included in the model (R6 and R7). The significance of these reactions for the simplified model relies partially on the fact that they compete with CO_2 decomposition reactions for the plasma

electrons, causing the CO_2 conversion to flatten as the O_2 and O_3 densities increase. Among the ionic and neutral reactions, recombination processes of O atoms (or anions) with CO to form CO_2 are also part of the reaction set. Likewise, these reactions contribute to flatten the conversion of CO_2 at long residence times [31]. For further details on this model and its validity, refer to [31].

Table 1 - Reduced reactions set. All rate constants in cm^3s^{-1} unless indicated otherwise.

No.	Reaction	Rate constant	Reference	Note
R1	$e + CO_2 \rightarrow e + e + CO_2^+$	f(σ)	[45]	1
R2	$e + CO_2 \rightarrow CO + O + e$	f(σ)	[45]	1
R3	$e + CO_2 \rightarrow CO + O^-$	f(σ)	[45]	1
R4	$e + O_3 \rightarrow O + O_2 + e$	f(σ)	[46]	1
R5	$e + O_2 \rightarrow e + O + O$	f(σ)	[45]	1
R6	$e + O_2 \rightarrow O + O^-$	f(σ)	[45]	1
R7	$e + O_2 + M \rightarrow O_2^- + M$	f(σ)	[46]	1,2
R8	$O^- + CO \rightarrow e + CO_2$	6.50×10^{-10}	[31]	-
R9	$O^- + O_2 \rightarrow e + O_3$	1.00×10^{-12}	[31]	-
R10	$O^- + O_3 \rightarrow e + O_2 + O_2$	3.00×10^{-10}	[31]	-
R11	$e + CO_2^+ \rightarrow CO + O$	6.50×10^{-07}	[31]	-
R12	$O_2^- + CO_2^+ \rightarrow CO + O_2 + O$	6.00×10^{-07}	[31]	-
R13	$O + O + M \rightarrow O_2 + M$	$5.2\times10^{-35}e^{(900/T[K])}$	[31]	2
R14	$O + O_2 + M \rightarrow O_3 + M$	$4.5\times10^{-34}\,(T[K]/298)^{-2.70}$	[31]	2
R15	$O + O_3 \rightarrow O_2 + O_2$	$8.0\times10^{-12}e^{(-17.13/T[K])}$	[31]	-
R16	$O + CO + M \rightarrow CO_2 + M$	$1.7\times10^{-33}e^{(-1510/T[K])}$	[31]	2
R17	$O_3 + M \rightarrow O_2 + O + M$	$4.1\times10^{-10}e^{(-11430/T[K])}$	[31]	2

1. Rate coefficient calculated by BOLSIG+ solver for a given EEDF.
2. Three-body process, rate coefficients in cm^6s^{-1}

2.8. Vibrationally excited states of CO_2

The role of vibrationally excited states of CO_2 in its dissociation and the decision to exclude them from the chemistry set is addressed in this section. A fluid model for CO_2 dissociation

reactions in a parallel DBD reactor including an extensive description of the vibrational kinetics can be found in [47]. Treanor *et al.* [48] showed that under conditions characterised by a vibrational temperature well greater than the translational temperature, a population inversion in the energy levels can be achieved. Therefore, as discussed in [33,43], these largely populated highly excited anharmonic vibrational levels are deemed crucial for the dissociation of the CO_2 molecule. In this regard, a study of the vibrational distribution function for CO_2 comparing MW and DBD discharges (at 20 Torr and atmospheric pressure, respectively) can be found in [33]. According to their results, the population of high vibrational states is a result of the rates of (or the competition between) the different processes involved, namely, electron impact vibrational excitation (exciting CO_2 molecules), vibrational-vibrational exchange collisions (which favour highly excited states) and vibrational-traslational relaxations (which de-excite vibrationally excited CO_2 molecules as it thermalises the gas). In addition, there are factors that favour or impede the different mechanisms involved. For instance, a long duration of a plasma pulse will favour vibrational excitations as it implies availability of free energetic electrons. On the other hand, a high pressure will contribute to the de-excitation of CO_2 molecules back to their ground state. Indeed, it is concluded that the pressure enhances the reaction rate of vibrational-translational (VT) transitions as collisions with ground state CO_2 molecules are more likely [33].

Interestingly, MW discharges represent a plasma duration in the order of the milliseconds (far greater than DBD in the order of nanoseconds) and are usually performed at low pressures, which favours largely populated high vibrational states that can certainly lead to dissociation. On the other hand, DBD discharges are often performed at atmospheric pressure so the vibrational-translational relaxations are orders of magnitude faster than in a low pressure MW discharge (in a DBD reactor, vibrationally excited states can thermalise in a few microseconds). Moreover, DBD microdischarges last for a very short time (in the order of nanoseconds), which is detrimental for the electron impact vibrational excitations. The vibrational excitation gained in a microdischarge (lasting for nanoseconds) is then thermalised (lost) before the next microdischarge takes place (after several microseconds). These factors explain why long-lasting large populations of high vibrational states are not achieved in DBD discharges, thus CO_2 dissociation must proceed through other mechanisms such as electronic excitations [33].

2.9. Plasma kinetic model – cross sections data

The rate coefficients for electron impact reactions were calculated by the Boltzmann solver BOLSIG+ [40] implemented in the ZDPlasKin Fortran module as a function of the corresponding cross sections. Cross section data was retrieved from different databases within the LXCat project [41]. It should be highlighted that the Electron Energy Distribution Function (EEDF) was calculated based on complete and consistent (whenever possible) sets of cross sections for each involved species. The complete and consistent IST-Lisbon Database reported in [37] and available in LXCat ([41]) was used for CO_2 and O_2 processes. Importantly, this cross section data has been validated against measured swarm data [37]. For CO, O_3 and O species, complete cross section data sets from Morgan database were adopted [46]. The cross sections for the three body recombination R7 were also taken from the latter database. With all this data, the EEDF was calculated and then used to integrate the corresponding cross sections in order to obtain the rate coefficients of the electron impact reactions included in the model (R1 to R7). Specific references to the databases can be found in Table 1 and a list of the collisional processes considered for the calculation of the EEDF is included in the Supporting Information (Table S4).

Regarding the completeness of the IST-Lisbon database for CO_2 processes, it should be noted that only one superelastic collisional process in included, namely, de-excitation from $v_1 \equiv (010)$ to the ground level, v_0. This is the dominant de-excitation process while a second superelastic process would be required for a better accuracy of the calculated swarm parameters at reduced electric fields below ~1 Td [37], which is not the case in this study. In addition, the effect of the superelastic process $v_1 \rightarrow v_0$ is particularly important at low electric fields but barely noticeable above 10 Td [37], while our work considers 56 Td.

Although the superelastic collision $v_1 \rightarrow v_0$ is included in the set, the number density of $CO_2(v_1)$ will always be zero since vibrationally excited states of CO_2 were not considered in this model (see Section 0). Thus, this superelastic collision will never account for an energy gain towards the EEDF. To assess the impact of this approximation, the EEDF calculated with BOLSIG+ for the case of this study (no $CO_2(v_1)$) was compared with that obtained for a relative $CO_2(v_1)$ population of 0.076 at 300K, according to [37]. The results indicate that EEDFs considering superelastic collisions tend to be slightly shifted towards higher electron

energies (as these processes can effectively transfer energy back to the electrons). Then, our approximation could result in a minor underestimation of the electron impact rate coefficients. However, the effect of superelastic collisions in the EEDF vanishes for reduced electric fields beyond 10 Td and this approximation is considered suitable for our work. A comparison of the calculated EEDFs, electron energies and rate coefficient for both cases at different electric fields can be found in the Supporting Information (Figures S1-S5 and Table S4).

The rate coefficient for CO_2 dissociation through electron impact excitation deserves a special mention as this process has been reported to be the dominant mechanism for CO_2 conversion in DBD reactors [32]. Hence, the cross section data employed for its calculation is a crucial factor for the validity of the model and the results obtained. Numerous cross section data sources are available for the CO_2 electron impact excitation and the direct association of these processes with CO_2 dissociation has been extensively studied in [32] and [37]. To start with, the IST-Lisbon dataset is based on the excitation processes described by Phelps [49], with thresholds of 7 and 10.5 eV. These cross sections have been extended to a wider range of electron energy as described in [45]. However, these cross sections are likely to involve more processes than only dissociation, as explained in [37]. Then, assigning Phelps's 7 and 10.5 eV cross sections to CO_2 dissociation is not straightforward and may result in an overestimation of the dissociation rate coefficients, as proved in [32] and [37]. On the other hand, Itikawa's Database ([50]), also available in LXCat, has been widely used in studies involving zero-dimensional plasma kinetic models [28–31]. However, this dataset has been recently reported to underestimate the CO_2 dissociation reaction rate coefficients [32,37]. Besides, Polak and Slovetsky's cross sections [38] have been reported to satisfactorily represent CO_2 dissociation. In this theoretical study, the authors described a total dissociation cross section showing two energy thresholds, in a similar fashion as Phelps's 7 and 10.5 eV datasets. Regardless of the shape, Polak's cross sections are much smaller in magnitude than those of Phelps, which could contribute to compensate the overestimation reported for the latter dataset [32,37]. Among these and other excitation cross sections, Phelps's 7 eV and Polak's datasets appear to be the most suitable to model CO_2 dissociation, according to results in [32] and [37], respectively.

In this work, the recommendation given by the authors of the IST-Lisbon Database was followed [37]. Therefore, Polak and Slovetsky's CO_2 dissociation total cross section data was used to calculate the CO_2 dissociation rate coefficient (R2). Nevertheless, these cross sections were integrated over the EEDF calculated with the IST-Lisbon Database complete and consistent set of cross sections (excluding Polak's cross sections).

3. Results and Discussion

3.1. Validation of the model – average electron density

The averaging procedure described in section 2.5 has been verified with the calculation described below. A simulation of one single filament has been performed, involving 662 micro-discharges (modelled as 30 ns-long pulses) repeated every 55.6 μs ($\Delta t_{micro-discharge}$). Then, each micro-discharges has an afterglow of (55.6 μs - 30 ns) seconds. This $\Delta t_{micro-discharge}$ corresponds to a frequency of 9 kHz (that of the applied voltage) and covers a reaction time of 3.67×10^{-2} seconds, i.e. Δt_{fil} in this verification ($\Delta t_{micro-discharge} \times num_{microdischarges}$). This $num_{microdischarges}$ and Δt_{fil} corresponds to the calculations with a flow rate of 25 mL/min. The electron density in this case was a function of time peaking at 1×10^{13} cm^{-3} in an interval of 30 ns, as described in section 2.5. Then, the conversion computed by such calculation was compared with that of a calculation consisting of an average electron density of 4×10^{9} cm^{-3} (as found in section 2.5) kept constant for 3.67×10^{-2} seconds. The results are 0.3029 % and 0.3028 %, respectively. The absolute error is 0.0001 % while the relative error equals 0.0003 (0.03%). Therefore, it can be concluded that this approximation is reliable for the conditions being addressed in this paper. This involves low temperatures (300 K) and low conversion values, where the chemistry of the system is not too complex and the contribution of reactions between heavy particles in the afterglow is orders of magnitude smaller than that of electron impact processes during the pulse.

The computational time saved through this approximation outweighs any concern about the already negligible error introduced by it. The first calculation (662 pulses) ran for 7.5 hours, that is, 450 minutes. By contrast, it took less than a minute to complete the averaged

calculation, therefore resulting in a time saving of more than 99%. Thus, we consider this approximation not only reliable but also necessary within this particular framework.

3.2. Validation of the model – matching experimental data

The validity of the model is only achieved once its results are contrasted with the experimental measurements it intends to represent. Selectivity towards CO varies around 96-98 % for every case, making it useless to compare laboratory measurements with the model results. Therefore, only CO_2 conversion will be used to match the experimental and calculated values. Overall, for the model proposed in this work, the calculated conversion figures are in very good agreement with the experimental data, with only one measurement having a relative error above 5%. The complete set of results including every calculation is presented in Table 2.Table 2 - Results. In addition, results are displayed graphically in Figure 3 and Figure 4 for variable power and flow rate figures, respectively. Combined results in terms of SEI (specific energy input, defined as the ratio between the power and the flow rate) are presented in Figure 5. The definitions of the variables used to process the data are as follows.

$$Conversion\ (\%) = \frac{CO_2\ Converted\ (\frac{Mol}{s})}{CO_2\ Input\ (\frac{Mol}{s})} \quad (12)$$

$$SEI\ (J/mL) = \frac{Power\ (W) \times \frac{60\ s}{1\ min}}{Flow\ rate\ (\frac{mL}{min})} \quad (13)$$

$$Energy\ Efficiency\ (\%) = \frac{CO_2\ Converted\ (\frac{Mol}{s}) \times \Delta H°_{CO_2 Splitting} (\frac{J}{mol})}{Power\ (W)} \quad (14)$$

Where the reaction enthalpy of the CO_2 decomposition reaction is $\Delta H°_{CO_2 Splitting} = 280 \frac{KJ}{mol}$

3.2.1 Effect of discharge power

As can be seen graphically in Figure 3, the calculated conversion curve over power variations seems to satisfactorily represent the experimental data. The major deviation is found at 50 W (SEI = 120 kJ/L, see Figure 3), where the calculated conversion is 0.3% greater (a relative error of 1.3%). It is expected that higher power values lead to inaccuracies in the model as it

is not able to predict saturation. In fact, a similar behaviour has been reported previously for SEI figures above 100 kJ/L [31]. However, the system becomes inefficient beyond that SEI value. The model has been optimized for the range of parameters that yield relatively high efficiencies, while deviations are expected to occur outside those ranges. Indeed, the range of applicability of this model covers the most relevant operating conditions in terms of energy efficiency. As regards conversion, it is noticeable that values up to around 20% can be modelled accurately with the current reduced chemistry set, as opposed to the reported limit of 15% [31]. This difference may be related to the chosen Polak's cross sections for the electron impact CO_2 dissociation reaction as it affects the relative contribution of the different processes leading to CO_2 splitting.

Table 2 - Results. All calculations with i.d. (quartz tube) = 22 mm, o.d. (high voltage electrode) = 17 mm, gap = 2.5 mm, length = 100 mm.

Flow rate	**Power**	**SEI**	**EXP. CO_2 Conversion**	**MODEL CO_2 Conversion**	**Relative error [1]**	**EXP. Efficiency**	**MODEL Efficiency**
mL/min	**W**	**kJ/L**	**%**	**%**	**%**	**%**	**%**
25.0	**10**	24	17.4	17.4	0.2	8.3	8.3
25.0	**20**	48	19.8	19.6	1.1	4.7	4.7
25.0	**30**	72	21.0	20.9	0.3	3.3	3.3
25.0	**40**	96	22.0	22.0	0.2	2.6	2.6
25.0	**50**	120	22.4	22.7	1.3	2.1	2.2
25.0	50	120	22.4	22.7	1.3	2.1	2.2
31.2	50	96	20.8	20.9	0.3	2.5	2.5
41.2	50	73	18.0	18.8	4.7	2.8	2.9
62.5	50	48	15.8	16.0	1.5	3.7	3.8
125.0	50	24	12.6	12.0	5.5	6.0	5.7

1. The relative error is defined as the difference between the experimental and model conversions divided by the average of both.

3.2.2 Effect of flow rate

On the other hand, the model provides acceptable yet less satisfactory results for the calculations involving variable flow rate. In most cases, the calculated results seem to overestimate the CO_2 conversion. It can be seen in Figure 4 that this positive error is balanced by a negative error as the flow rate grows. In fact, the conversion for 125 mL/min is indeed underestimated by 0.6 % (relatively, 5.5 %). Overall, these results are deemed to be acceptable in terms of variable flow rate.

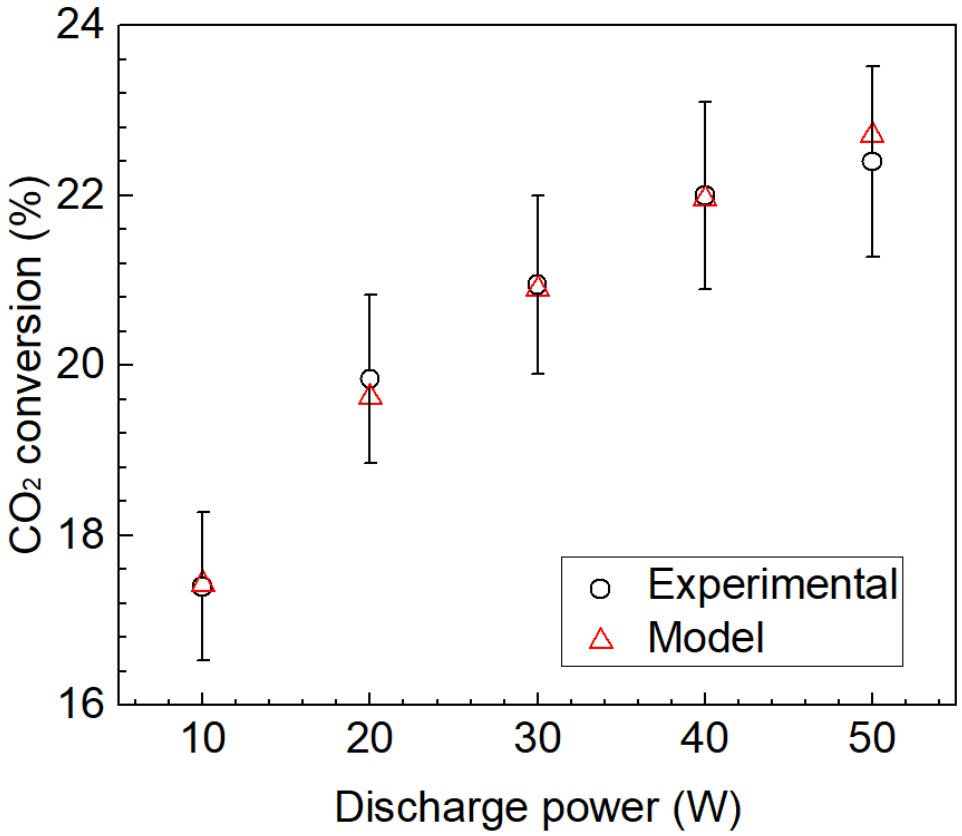

Figure 3 – CO_2 conversion at different discharge powers and 25 ml/min.

3.2.3 Overall results

According to our results, this model has proved to accurately represent the chemistry of the system up to conversion values of around 20%, with power values ranging from 10 up to 40 W. However, the remaining calculation with variable power (50 W) results in a conversion figure that is slightly higher than the experimental one. In addition, almost every calculation with variable flow rate shows discrepancies with the laboratory measurements, regardless of the conversion value (all of them considering 50 W).

Overall, the proposed model presents a reasonable agreement with the experimental measurements in terms of CO_2 conversion for the full range of experimental measurements taken into account. Thus, this validates the model and indicates it is reliable enough so as to analyse the reaction mechanism based on its results (see Section 3.3).

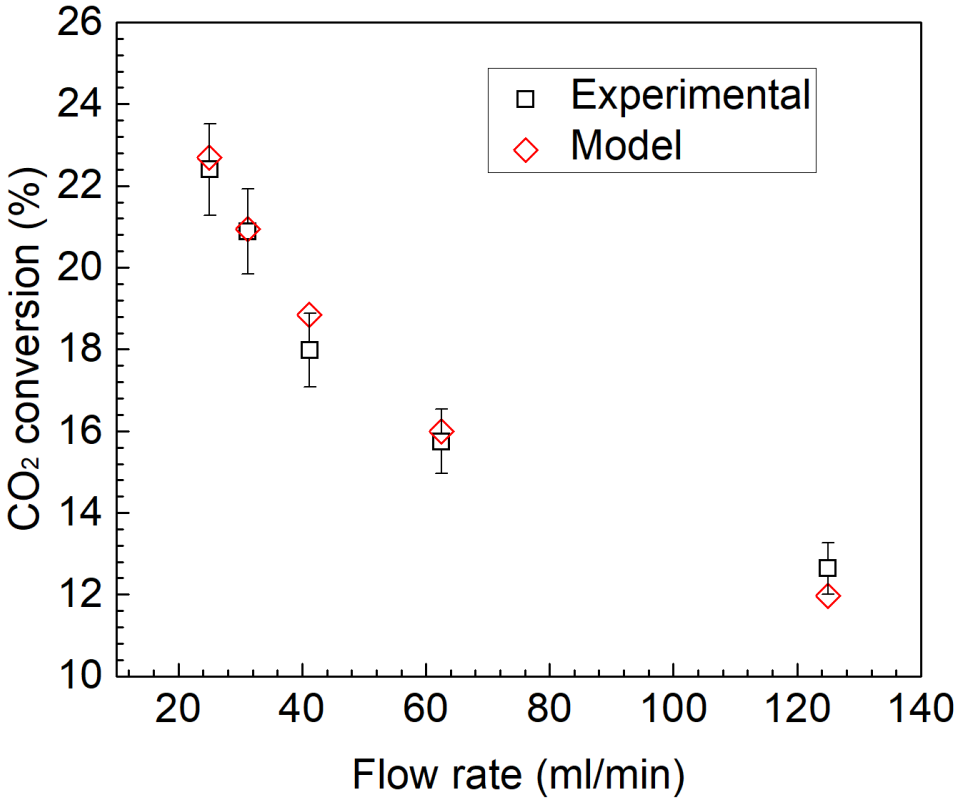

535

536 *Figure 4 – CO_2 conversion at different flow rates and 50 W.*

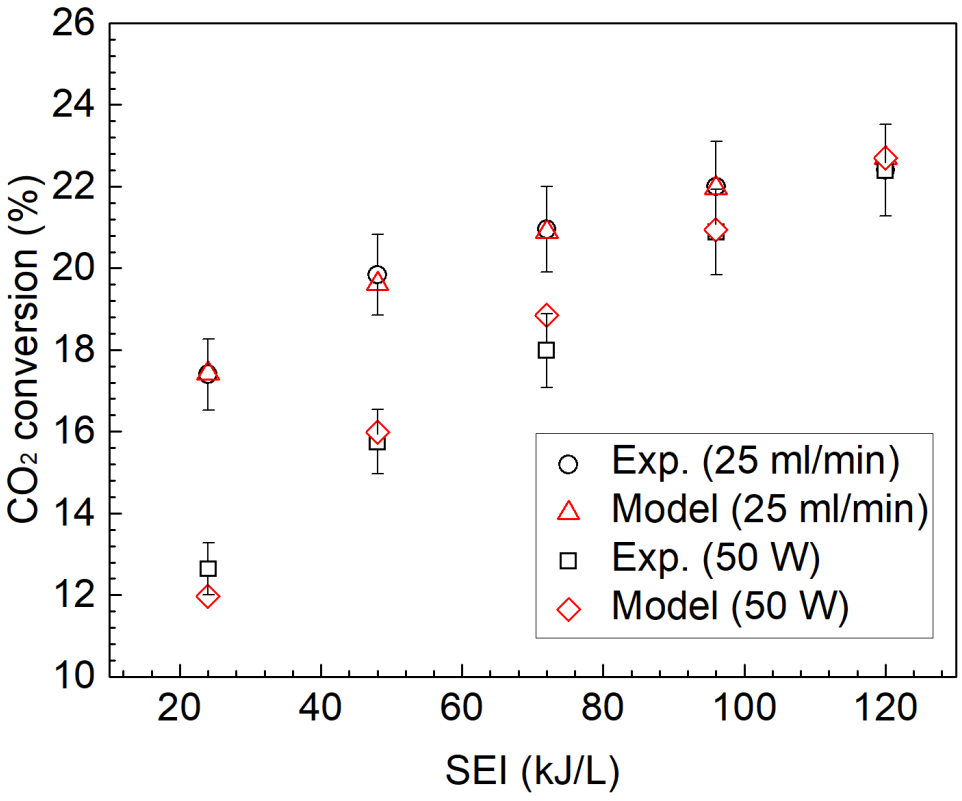

537

538 *Figure 5 – CO_2 conversion at different SEI values by changing discharge power or CO_2*
539 *flow rate.*

540

541 ### 3.3. Reaction pathways analysis

542 As mentioned above, in this study we employed a reduced chemistry set for the conversion
543 of CO_2 developed and reported in [31], consisting of 9 species and 17 reactions (see Table
544 1). Such simplification may lose reliability at higher conversion values as the chemistry of
545 the system becomes more complex and neglected reactions become relevant. However, it
546 seems that point has not been reached in this study. According to our results, the entire range
547 of conversion covered by the experiments in [36] is well reproduced by the calculations
548 yielding a reasonable agreement in every case.

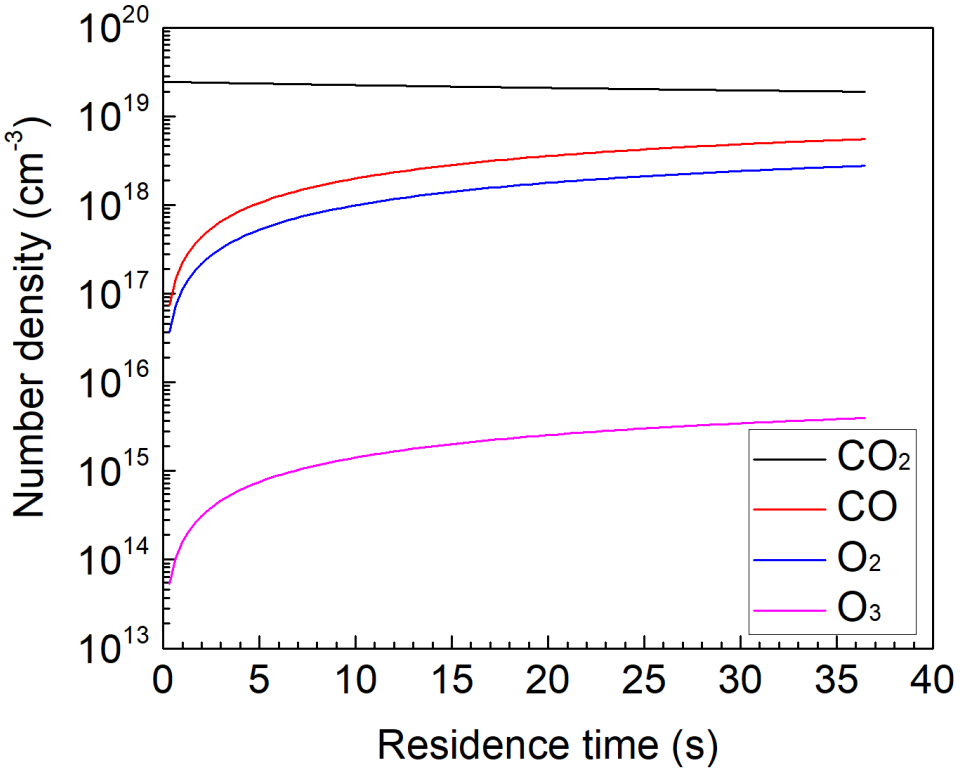

549
550 *Figure 6 – Number density of CO_2, CO and O_2 and O_3 (25 mL/min and 50 W)*

551

552 As the experiments intended to model were performed at atmospheric pressure and ambient
553 temperature, the initial CO_2 number density is set to 2.45×10^{19} cm^{-3} in all cases. This figures

drops to 1.89 $\times 10^{19}$ cm^{-3} for the highest conversion achieved (22.7%). The main products of these reactions are CO and O_2, with final number densities of about 5.56×10^{18} cm^{-3} and 2.77×10^{18} cm^{-3}, respectively (also for a conversion of 22.7%). The major by-product is O_3, several orders of magnitude below the final density of O_2 (3.96×10^{15} cm^{-3}). These results are illustrated in Figure 6.

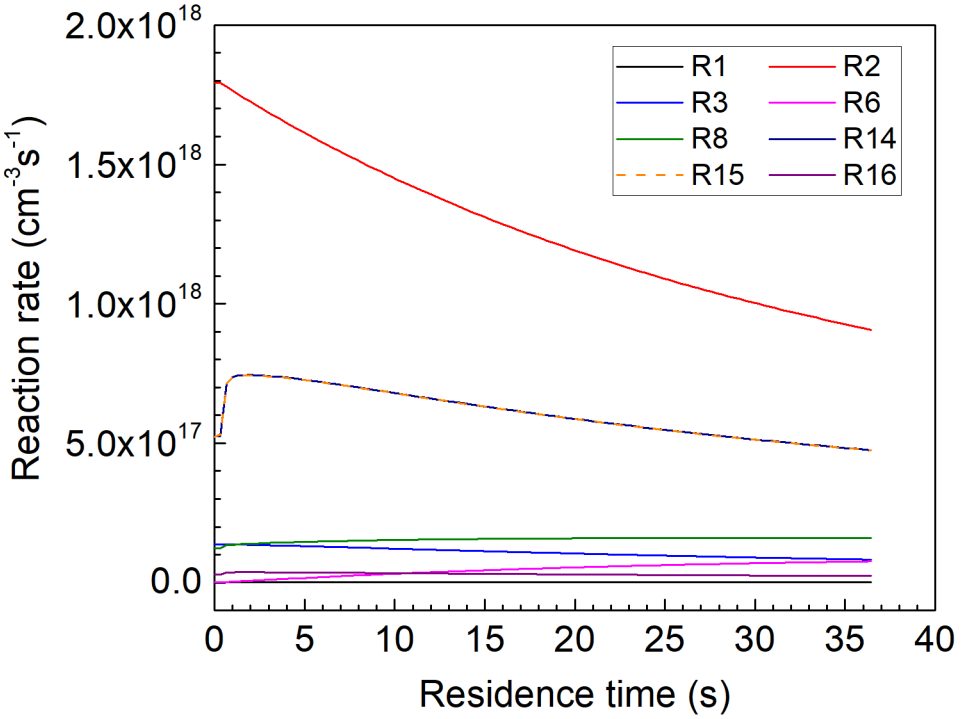

Figure 7 - Reaction rate of main reactions (25 mL/min and 50 W)

Mechanisms for CO_2 splitting and recombination

As stated above, the reduced reactions set considered for this study includes three possible mechanisms for CO_2 decomposition, namely, electron attachment (R1), electron impact dissociation (R2) and electron impact total ionisation (R3). Their relative contributions to the observed conversion figures will be determined by their rate coefficients which in turn depend heavily on the cross sections used for each process. As it has been mentioned, Polak and Slovetsky's cross sections were used for the electron impact dissociation [38] while the IST-Lisbon database available in LXCat were used for the remaining two reactions [45]. With these cross sections, the BOLSIG+ solver predicts that the highest rate coefficient is

that of the electron impact dissociation, R2 (around 1.9×10^{-11} cm^3s^{-1} for initial conditions). The electron attachment reaction (R3) has a rate coefficient of around 9.1×10^{-13} cm^3s^{-1} at initial conditions while that of the total ionisation (R1) is even an order of magnitude lower (2.9×10^{-14} cm^3s^{-1}). With these results, it can be concluded that the electron impact dissociation is the dominant mechanism for CO_2 splitting accounting for around 95% of the conversion. The electron attachment represents the remaining 5% while the contribution of the total ionisation to the CO_2 conversion is negligible (see Figure 7 for a comparison between reaction rate values). This is in qualitative agreement with the results reported by Ponduri *et al*. [47], while the relative contribution of each dissociation channel changes quantitatively. The latter study consists of a DBD time- and space-dependent fluid model including an exhaustive description of the vibrational kinetics of CO_2. The authors also conclude that the electron impact dissociation represents the main channel for CO_2 dissociation, accounting for approximately 80% of the CO production. In addition, our results qualitatively agree with [32,37]. These DBD models predicted a more balanced contribution of these processes as a result of the cross sections used [28–31]. It should be mentioned that the study from where the reduced set of reactions was taken ([31]) used Itikawa's dataset, as stated in [32]. As described in Section 2.9, this database has been proven to underestimate the electron impact dissociation rate coefficient (compared to the Polak's dataset to be used in this study), making its contribution comparable to that of the total ionisation reaction.

It should be highlighted that the reduced electric field in all these calculations is 56 Td according to the experimental measurements (Lissajous figures) [36,42]. This yields an average electron energy of around 2.21 eV. According to the literature, the contribution of the total ionisation overtakes that of the electron attachment by several orders of magnitude at higher E/N values, which are out of the scope of this work [32].

The CO produced is rather stable in the plasma and therefore it is the major product of this reaction. Nevertheless, this molecule does take part in some recombination reactions (R8 and R16). The recombination with oxygen anions (O^-, R8) accounts for 73% of the CO loss processes, whereas the three-body recombination with O radicals represents the remaining 27%. See Figure S5 for a comparison between the reaction rates of minor contributing reactions (excluding R2, R14 and R15).

Regarding O radicals, the recombination with CO molecules (R16) is not their main consumption mechanism as its rate coefficient is one order or magnitude lower than that of other processes involving these species. After an initial prevalence of reaction R13 which builds up an initial O_2 density, reactions R14 and R15 take over. These reactions require an initial concentration of O_2 and O_3 to occur and became preponderant once achieved. Their reaction rates are almost indistinguishable from one another, both being in and around ~ 6×10^{17} $cm^{-3}s^{-1}$ (see Figure 7). These two reactions with high rates explain the formation of O_2 in this chemistry set. The main reaction mechanisms within this chemistry set are depicted in Figure 8, where black arrows represent CO production while blue ones denote O_2 production. Recombination reactions are indicated with red arrows.

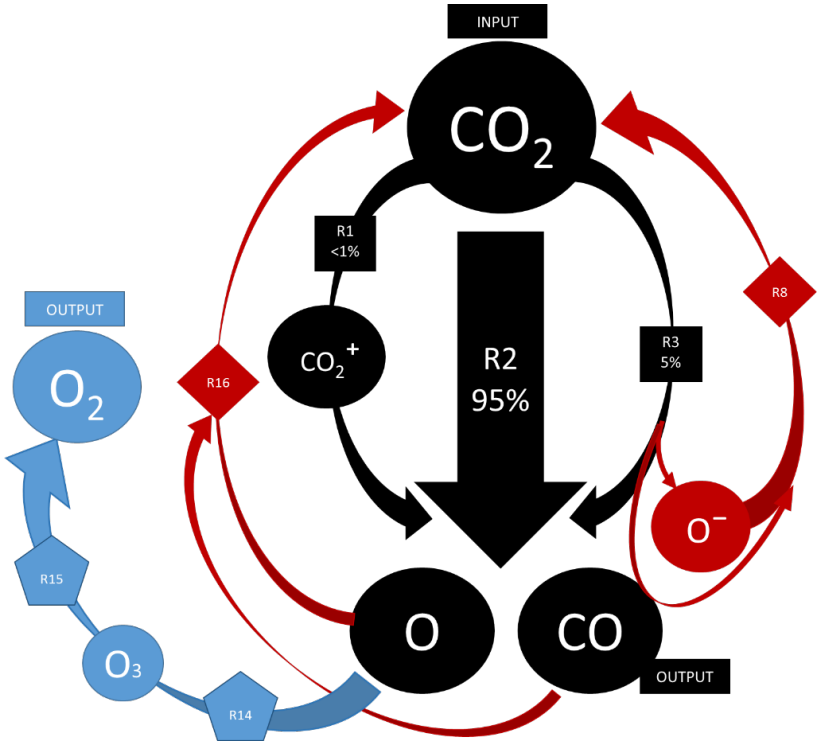

Figure 8 - Scheme of the proposed reaction mechanism

3.4. Energy efficiency

A discussion on the energy efficiency of this system is presented in this section. The values obtained for these experiments and calculations are presented in Table 2 and shown in Figure

9. An analysis of the agreement between the model and the experimental results will not be included as it is essentially the same as that of the conversion, already addressed above. By contrast, it is relevant to compare the efficiency values obtained with what has been previously reported for CO_2 splitting in DBD reactors, as well as to discuss the potential reasons for the efficiency achieved.

DBD reactors are known for their low efficiency in CO_2 splitting reactions, rarely exceeding 10%. An exhaustive collection of data on DBD energy efficiency can be found in [26,27]. The values presented in this work fit within that description and also the decrease in the efficiency as the SEI grows is also consistent with the literature. A maximum efficiency of 8.3% was found in this work for a rather low conversion of 17.4%. For higher conversion values, the efficiency drops down to, for instance, 2.2% at a conversion of 22.7%. The dependence of the efficiency with the power seems to be somewhat stronger than with the flow rate. A further analysis of these values can be found in the study from where the experimental data has been taken [36]. In the next section, a discussion about the role of the different factors that are believed to affect the energy efficiency of the CO_2 splitting process is presented (a necessary comparison between MW and DBD discharges is also included).

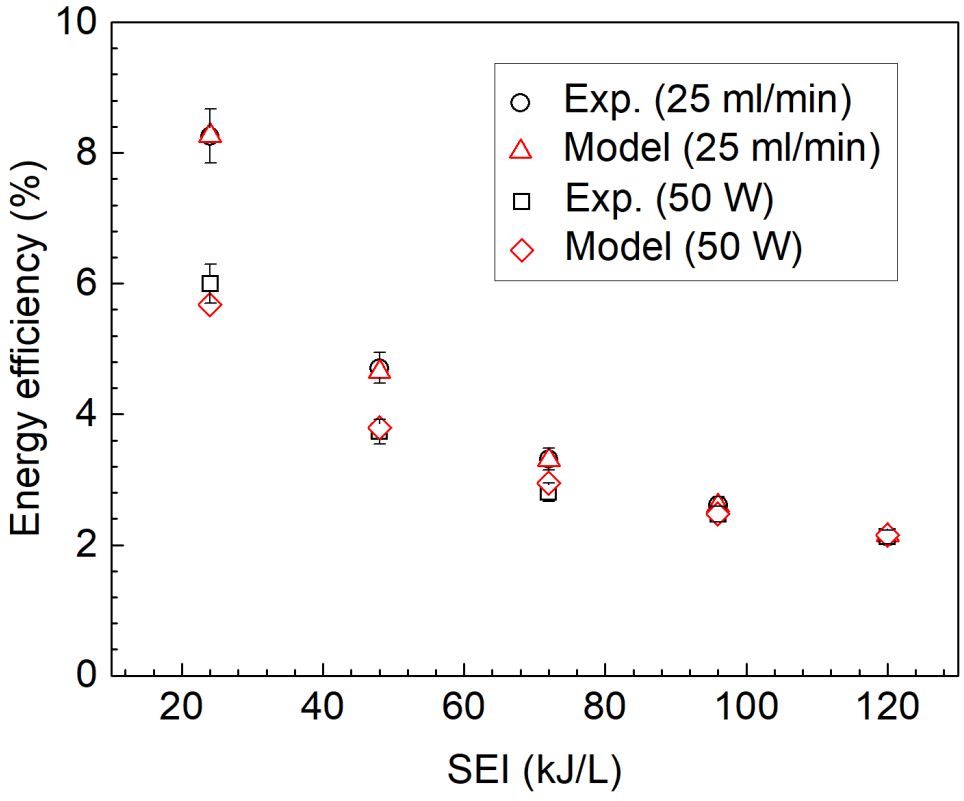

Figure 9 - Energy Efficiency at different SEI by changing discharge power or CO_2 flow rate.

3.5. Reduced electric field and vibrationally excited states

As opposed to DBD reactors, MW normally show a greater energy efficiency, varying from around 10% up to even 90% [26,27] (see the effect of the operating pressure below). It is often claimed that the reason for the difference in their efficiencies is the range of reduced electric fields they work on, placing vibrationally excited states of CO_2 as the main channel for dissociation in MW discharges. While DBD reactors have been reported to operate at high reduced electric fields (E/N), in the order of 200 Td; MW discharges exhibit a smaller E/N, around 50 Td [31,33]. Indeed, it can be seen in Figure 10 that most of the electron energy is consumed towards electronic vibrational excitation processes at 50 Td, while the relevance of these processes is negligible at higher E/N. At around 200 Td, the vast majority of the electron energy is directed to electron impact excitations (see Figure 10, calculated by BOLSIG+ with the cross-section data sets used in this work). Then, the high efficiency of the MW discharges has been associated with the low E/N figures while the low efficiency in DBD reactors has been linked to the lack of vibrational excitation due to the higher E/N [28,31,33,34].

However, the latter argument about the lack of vibrational states at ~200 Td cannot explain the low efficiency of, at least, this DBD reactor. As mentioned above, the reduced electric field used in this work is 56 Td, calculated from experimental measurements obtained through Lissajous Figures (method described in [42] applied to our previous work [36]). The method employed allows measurement of the voltage across the gap, importantly excluding the voltage drop through the dielectric barrier. It is important to notice that this value is in the order of those associated with MW discharges and differs considerably from 200 Td, reported elsewhere and thought to characterise DBD discharges [31,33].

At this point it is important to notice that the high efficiencies achieved by MW discharges require this reactor to be operated at low pressure. Moreover, when these discharges are performed at atmospheric pressure, their efficiency drops significantly to values slightly

greater than those of DBD discharges (for a collection of data from different experimental works, see [26,27]). Then, it is apparent that the pressure plays a role in the efficiency of the CO_2 splitting reaction. In this regard, it has been theoretically shown in [51] that the highest conversions and energy efficiencies of CO_2 splitting reactions performed on MW discharges are achieved at 300 mbar, which is in agreement experimental results. Moreover, as stated in Section 0, long-lasting large populations of high vibrational states are not achieved in DBD reactors as the vibrationally excited molecules thermalise before the next micro-discharge occurs, as a result of the combination of high pressure and low duration of plasma that characterises these types of discharges [33].

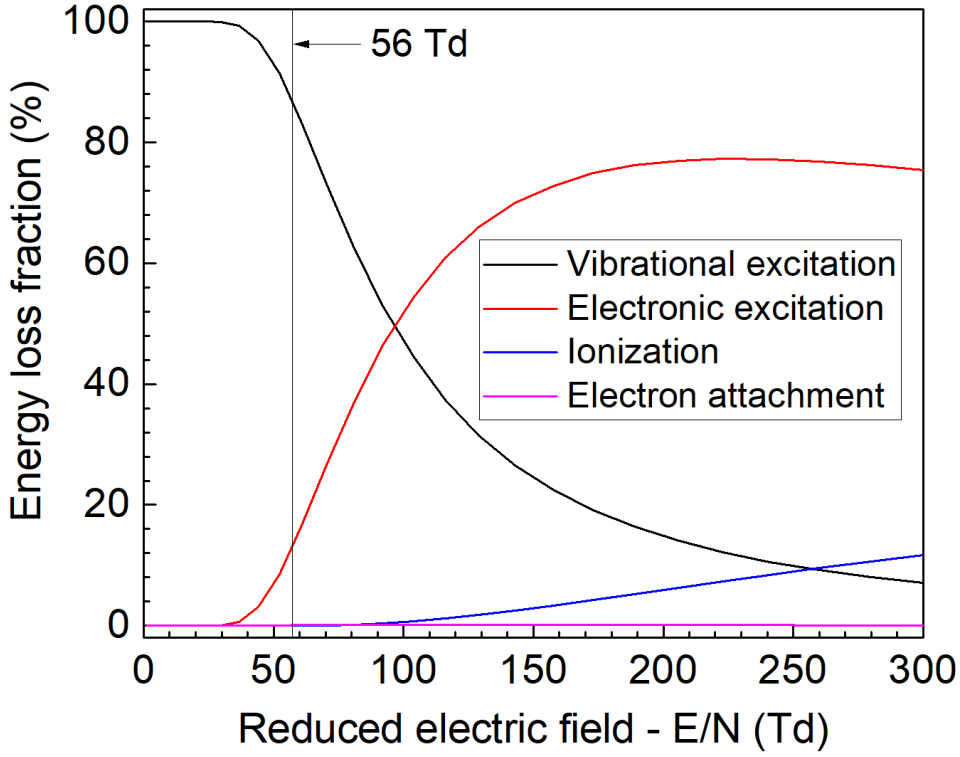

Figure 10 - Energy loss fractions towards different electron impact processes as a function of E/N, calculated by BOLSIG+ with the cross-sections used in this study.

The present work can now be regarded with these very important results in mind. According to Figure 10, at 56 Td, most of the energy imparted to the electrons by the plasma is directed towards vibrational excitation. For that reason, we believe that vibrational excitation does indeed take place in DBD reactors, although leading to de-excitation rather than dissociation, due to the characteristic pressure and plasma duration of these discharges. Then, the low energy efficiency achieved in this work (and other DBD discharges) seems reasonable as

vibrational excitation consumes ~ 90% of the energy imparted by the plasma and is not translated into CO_2 conversion. In other words, ~ 90% of the energy given to the system is lost in a vibrational excitation – de-excitation sequence. Moreover, very little energy (just above 10%) is transferred to electronic excitation of CO_2, which has been shown in this work (section 3.3) to be the main contributor to the dissociation process.

Finally, through this discussion, we can validate our approach of considering vibrational excitations for the calculations of the EEDF, but not including reactions between vibrationally excited states in the chemistry set as a channel for CO_2 dissociation.

4. Conclusions

In this work, we proposed a novel approach to the already existing zero-dimensional DBD plasma kinetic models in order to include the effect of experimental parameters as discharge power and flow rate. In addition, an average electron density calculated over hundreds of microdischarges was used as an approximation, resulting in a great reduction of the computational cost implied within this particular framework. Our DBD model was applied to CO_2 splitting reactions and contrasted with readily available experimental data covering a range of power and flow rate figures. A reduced chemistry set for CO_2 dissociation reactions was employed [31], together with Polak and Slovetsky's cross section data for the CO_2 electron impact dissociation rate coefficient [38].

Overall, the results of this model represent the experimental measurements accurately within the whole range of operational parameters tested, with a maximum relative error of around 5.5%. Upon this validation of the model, the underlying chemistry and reaction mechanisms involved in the CO_2 conversion were analysed. Our results indicate that, under the operational conditions considered in this work, the electron impact dissociation constitutes the dominant mechanism for the CO_2 splitting, accounting for 95% of the CO_2 conversion. Finally, some insights on the underlying reasons of the low energy efficiency shown by DBD reactors are given. Our results, coupled with important findings published elsewhere [33], suggest that most of the energy input is wasted towards vibrational excitations that have already been proven not to lead to CO_2 dissociation under conditions of short exposure to plasma electrons and atmospheric pressure, which characterise DBD reactors.

Acknowledgement

We acknowledge the European Union (EU) and Horizon 2020 funding awarded under the Marie Skłodowska-Curie action to the EUROPAH consortium (grant number 722346).

References

[1] C. Liu, G. Xu, T. Wang, Non-thermal plasma approaches in CO2 utilization, Fuel Process. Technol. 58 (1999) 119–134. doi:10.1016/S0378-3820(98)00091-5.

[2] R. Snoeckx, A. Bogaerts, Plasma technology – a novel solution for CO2 conversion?, Chem. Soc. Rev. 46 (2017) 5805–5863. doi:10.1039/C6CS00066E.

[3] R. Bennett, S. Clifford, K. Anderson, G. Puxty, Carbon Capture Powered by Solar Energy, Energy Procedia. 114 (2017) 1–6. doi:10.1016/j.egypro.2017.03.1139.

[4] Y. Tan, W. Nookuea, H. Li, E. Thorin, J. Yan, Property impacts on Carbon Capture and Storage (CCS) processes: A review, Energy Convers. Manag. 118 (2016) 204–222. doi:10.1016/j.enconman.2016.03.079.

[5] A. Alonso, J. Moral-Vico, A. Abo Markeb, M. Busquets-Fité, D. Komilis, V. Puntes, A. Sánchez, X. Font, Critical review of existing nanomaterial adsorbents to capture carbon dioxide and methane, Sci. Total Environ. 595 (2017) 51–62. doi:10.1016/j.scitotenv.2017.03.229.

[6] I. Sreedhar, T. Nahar, A. Venugopal, B. Srinivas, Carbon capture by absorption – Path covered and ahead, Renew. Sustain. Energy Rev. 76 (2017) 1080–1107. doi:10.1016/j.rser.2017.03.109.

[7] M. Kumar, S. Sundaram, E. Gnansounou, C. Larroche, I.S. Thakur, Carbon dioxide capture, storage and production of biofuel and biomaterials by bacteria: A review, Bioresour. Technol. 247 (2018) 1059–1068. doi:10.1016/j.biortech.2017.09.050.

[8] M.S. Duyar, S. Wang, M.A. Arellano-Treviño, R.J. Farrauto, CO2utilization with a novel dual function material (DFM) for capture and catalytic conversion to synthetic natural gas: An update, J. CO2 Util. 15 (2016) 65–71. doi:10.1016/j.jcou.2016.05.003.

[9] N.A. Rashidi, S. Yusup, An overview of activated carbons utilization for the post-combustion carbon dioxide capture, J. CO2 Util. 13 (2016) 1–16. doi:10.1016/j.jcou.2015.11.002.

[10] S. Saeidi, N.A.S. Amin, M.R. Rahimpour, Hydrogenation of CO2to value-added products - A review and potential future developments, J. CO2 Util. 5 (2014) 66–81. doi:10.1016/j.jcou.2013.12.005.

[11] H. Abdullah, M.M.R. Khan, H.R. Ong, Z. Yaakob, Modified TiO2photocatalyst for CO2photocatalytic reduction: An overview, J. CO2 Util. 22 (2017) 15–32. doi:10.1016/j.jcou.2017.08.004.

[12] S. Paulussen, B. Verheyde, X. Tu, C. De Bie, T. Martens, D. Petrovic, A. Bogaerts, B. Sels, Conversion of carbon dioxide to value-added chemicals in atmospheric pressure dielectric barrier discharges, Plasma Sources Sci. Technol. 19 (2010). doi:10.1088/0963-0252/19/3/034015.

[13] S. Wang, Y. Zhang, X. Liu, X. Wang, Enhancement of CO2 Conversion Rate and Conversion Efficiency by Homogeneous Discharges, Plasma Chem. Plasma Process. 32 (2012) 979–989. doi:10.1007/s11090-012-9386-8.

[14] Q. Yu, M. Kong, T. Liu, J. Fei, X. Zheng, Characteristics of the decomposition of CO2in a dielectric packed-bed plasma reactor, Plasma Chem. Plasma Process. 32 (2012) 153–163. doi:10.1007/s11090-011-9335-y.

[15] F. Brehmer, S. Welzel, M.C.M. van de Sanden, R. Engeln, CO and byproduct formation during CO_2 reduction in dielectric barrier discharges, J. Appl. Phys. 116 (2014) 123303. doi:10.1063/1.4896132.

[16] D. Yap, J.M. Tatibouët, C. Batiot-Dupeyrat, Carbon dioxide dissociation to carbon monoxide by non-thermal plasma, J. CO2 Util. 12 (2015) 54–61. doi:10.1016/j.jcou.2015.07.002.

[17] K. Van Laer, A. Bogaerts, Improving the Conversion and Energy Efficiency of Carbon Dioxide Splitting in a Zirconia-Packed Dielectric Barrier Discharge Reactor, Energy Technol. 3 (2015) 1038–1044. doi:10.1002/ente.201500127.

[18] D. Mei, X. Zhu, C. Wu, B. Ashford, P.T. Williams, X. Tu, Plasma-photocatalytic conversion of CO2at low temperatures: Understanding the synergistic effect of plasma-catalysis, Appl. Catal. B Environ. 182 (2016) 525–532. doi:10.1016/j.apcatb.2015.09.052.

[19] T. Butterworth, R. Elder, R. Allen, Effects of particle size on CO2reduction and discharge characteristics in a packed bed plasma reactor, Chem. Eng. J. 293 (2016) 55–67. doi:10.1016/j.cej.2016.02.047.

[20] D. Ray, C. Subrahmanyam, CO_2 decomposition in a packed DBD plasma reactor: influence of packing materials, RSC Adv. 6 (2016) 39492–39499. doi:10.1039/C5RA27085E.

[21] D. Mei, Y.-L. He, S. Liu, J. Yan, X. Tu, Optimization of CO_2 Conversion in a Cylindrical Dielectric Barrier Discharge Reactor Using Design of Experiments, Plasma Process. Polym. 13 (2016) 544–556. doi:10.1002/ppap.201500159.

[22] S. Xu, J.C. Whitehead, P.A. Martin, CO2conversion in a non-thermal, barium titanate packed bed plasma reactor: The effect of dilution by Ar and N2, Chem. Eng. J. 327 (2017) 764–773. doi:10.1016/j.cej.2017.06.090.

[23] B. Ashford, X. Tu, Non-thermal plasma technology for the conversion of CO2, Curr. Opin. Green Sustain. Chem. 3 (2017) 45–49. doi:10.1016/j.cogsc.2016.12.001.

[24] Y. Uytdenhouwen, S. Van Alphen, I. Michielsen, V. Meynen, P. Cool, A. Bogaerts, A packed-bed DBD micro plasma reactor for CO 2 splitting : Does size matter ?, Chem. Eng. J. 348 (2018) 557–568. doi:10.1016/j.cej.2018.04.210.

[25] J.C. Whitehead, Plasma Catalysis: Known knowns... known unknowns... and unknown unknowns: Processing the research journey, J. Phys. D. Appl. Phys. 49 (2016) 243001. doi:10.1088/0022-3727/49/24/243001.

[26] M. Ramakers, G. Trenchev, S. Heijkers, W. Wang, A. Bogaerts, Gliding Arc Plasmatron: Providing an Alternative Method for Carbon Dioxide Conversion, ChemSusChem. 10 (2017) 2642–2652. doi:10.1002/cssc.201700589.

[27] W. Wang, D. Mei, X. Tu, A. Bogaerts, Gliding arc plasma for CO2conversion: Better insights by a combined experimental and modelling approach, Chem. Eng. J. 330 (2017) 11–25. doi:10.1016/j.cej.2017.07.133.

[28] R. Aerts, T. Martens, A. Bogaerts, Influence of Vibrational States on CO_2 Splitting by Dielectric Barrier Discharges, J. Phys. Chem. C. 116 (2012) 23257–23273. doi:10.1021/jp307525t.

[29] R. Snoeckx, R. Aerts, X. Tu, A. Bogaerts, Plasma-based dry reforming: A computational study ranging from the nanoseconds to seconds time scale, J. Phys. Chem. C. 117 (2013) 4957–4970. doi:10.1021/jp311912b.

[30] R. Snoeckx, M. Setareh, R. Aerts, P. Simon, A. Maghari, A. Bogaerts, Influence of N2concentration in a CH4/N2dielectric barrier discharge used for CH4conversion into H2, Int. J. Hydrogen Energy. 38 (2013) 16098–16120. doi:10.1016/j.ijhydene.2013.09.136.

[31] R. Aerts, W. Somers, A. Bogaerts, Carbon Dioxide Splitting in a Dielectric Barrier Discharge Plasma: A Combined Experimental and Computational Study, ChemSusChem. 8 (2015) 702–716. doi:10.1002/cssc.201402818.

[32] A. Bogaerts, W. Wang, A. Berthelot, V. Guerra, Modeling plasma-based CO2 conversion: Crucial role of the dissociation cross section, Plasma Sources Sci. Technol. 25 (2016). doi:10.1088/0963-0252/25/5/055016.

[33] T. Kozak, A. Bogaerts, Splitting of CO2 by vibrational excitation in non-equilibrium plasmas: A reaction kinetics model, Plasma Sources Sci. Technol. 23 (2014). doi:10.1088/0963-0252/23/4/045004.

[34] R. Snoeckx, A. Ozkan, F. Reniers, A. Bogaerts, The Quest for Value-Added Products from Carbon Dioxide and Water in a Dielectric Barrier Discharge: A Chemical Kinetics Study, ChemSusChem. 10 (2017) 409–424. doi:10.1002/cssc.201601234.

[35] A. Hurlbatt, A.R. Gibson, S. Schröter, J. Bredin, A.P.S. Foote, P. Grondein, D. O'Connell, T. Gans, Concepts, Capabilities, and Limitations of Global Models: A Review, Plasma Process. Polym. 14 (2016) 1–21. doi:10.1002/ppap.201600138.

[36] D. Mei, X. Tu, Conversion of CO2in a cylindrical dielectric barrier discharge reactor: Effects of plasma processing parameters and reactor design, J. CO2 Util. 19 (2017) 68–78. doi:10.1016/j.jcou.2017.02.015.

[37] M. Grofulović, L.L. Alves, V. Guerra, Electron-neutral scattering cross sections for CO2: A complete and consistent set and an assessment of dissociation, J. Phys. D. Appl. Phys. 49 (2016). doi:10.1088/0022-3727/49/39/395207.

[38] L.S. Polak, D.I.Y. Slovetsky, Excitation and Molecular Dissociation, Int. J. Radiat. Phys. Chem. 8 (1976) 257–282.

[39] S. Pancheshnyi, B. Eismann, G.J.M. Hagelaar, L.C. Pitchford, Computer code ZDPlasKin, http://www.zdplaskin.laplace.univ-tlse.fr (University of Toulouse, LAPLACE, CNRS-UPS-INP, Toulouse, France), (2008).

[40] G.J.M. Hagelaar, L.C. Pitchford, Solving the Boltzmann equation to obtain electron transport coefficients and rate coefficients for fluid models, Plasma Sources Sci. Technol. 14 (2005) 722–733. doi:10.1088/0963-0252/14/4/011.

[41] S. Pancheshnyi, S. Biagi, M.C. Bordage, G.J.M. Hagelaar, W.L. Morgan, A. V. Phelps, L.C. Pitchford, The LXCat project: Electron scattering cross sections and swarm parameters for low temperature plasma modeling, Chem. Phys. 398 (2012) 148–153. doi:10.1016/j.chemphys.2011.04.020.

[42] D. Mei, X. Zhu, Y.-L. He, J.D. Yan, X. Tu, Plasma-assisted conversion of CO_2 in a dielectric barrier discharge reactor: understanding the effect of packing materials, Plasma Sources Sci. Technol. 24 (2014) 015011. doi:10.1088/0963-0252/24/1/015011.

[43] A. Fridman, Plasma Chemistry, Cambridge University Press, 2008.

[44] L.-F. Dong, X.-C. Li, Z.-Q. Yin, S.-F. Qian, J.-T. Ouyang, L. Wang, Self-Organized Filaments in Dielectric Barrier Discharge in Air at Atmospheric Pressure, Chinese Phys. Lett. (2001) 1380.

[45] L.L. Alves, The IST-LISBON database on LXCat, J. Phys. Conf. Ser. 565 (2014). doi:10.1088/1742-6596/565/1/012007.

[46] Morgan database, www.lxcat.net, retrieved on January 2, 2018.

[47] S. Ponduri, M.M. Becker, S. Welzel, M.C.M. van de Sanden, D. Loffhagen, R. Engeln, Fluid modelling of CO2 dissociation in a dielectric barrier discharge, J. Appl. Phys. 119 (2016) 093301. doi:10.1063/1.4941530.

[48] C.E. Treanor, J.W. Rich, R.G. Rehm, Vibrational Relaxation of Anharmonic Oscillators with Exchange-Dominated Collisions, J. Chem. Phys. 48 (1968) 1798–1807. doi:10.1063/1.1668914.

[49] J.J. Lowke, A. V Phelps, B.W. Irwin, Predicted electron transport coefficients and operating characteristics of CO2–N2–He laser mixtures, J. Appl. Phys. 44 (1973) 4664.

[50] Itikawa database, www.lxcat.net.

[51] A. Berthelot, A. Bogaerts, Modeling of CO_2 Splitting in a Microwave Plasma: How to Improve the Conversion and Energy Efficiency, J. Phys. Chem. C. 121 (2017) 8236–8251. doi:10.1021/acs.jpcc.6b12840.